Infrared Physics and Technology 105 (2020) 103164

Contents lists available at ScienceDirect

Infrared Physics & Technology

journal homepage: www.elsevier.com/locate/infrared

Opto-mechanical temperature adaptability analysis of a dual-band IRSP for HWIL simulation

Yue Pan[a,*], Mai Hu[b], Xiping Xu[a], Yang Qiao[a]

[a] College of Optoelectronic Engineering, Changchun University of Science and Technology, 130022, Wei Xing Road 7089, Changchun, China
[b] Changchun Institute of Optics, Fine Mechanics and Physics, 130022, Dong Nanhu Road 3888, Changchun, China

ARTICLE INFO

Keywords:
Optical instruments
Infrared
Optomechanics
Thermal effects

ABSTRACT

The mid-wave and long-wave dual-band infrared scene projector (IRSP) is a practical instrument to test various infrared imaging systems in the experiment of hard-ware-in-the-loop (HWIL) simulation. It comprises two illumination modules and a telecentric projection module with dual field of view, covering atmospheric bands from 3.7 μm to 4.8 μm and 8 μm to 12 μm. In order to prevent the influence of temperature changes on the quality of projected images, the appropriate operating temperature range should be predicted during the development and design stages. In this paper, the integrated design of optical components is proposed, focusing on improving the temperature adaptability. Taking into account the different thermal environments faced by the illumination and the projection modules, opto-thermal analyses are carried out using finite element analysis (FEA) models respectively. According to the conditions of heat transfer, temperature field and the corresponding displacement field are calculated based on the quasi-static-processing approach. The least squares algorithm is adopted to fit the thermally induced deformation data for determining the Zernike polynomials of each lens's surface. And the optical performance of the IRSP is evaluated with the help of a ray-tracing software. The numerical simulations and the laboratory testing results show that the IRSP has good temperature adaptability in the temperature range from 10 °C to 35 °C.

1. Introduction

Dual-band infrared scene projectors used in hardware-in-the-loop (HWIL) simulation experiments, providing a series of simulated scenes that accurately reproduce the spectral, spatial, temporal, and radiant intensity characteristics of real world, and has been increasingly concerned to replace some high cost out-field tests of dual-band infrared imaging systems [1,2]. According to the working principle of the unit under test (UUT), dual-band IRSP should have the ability to control the radiant intensity in each band independently [3–7]. As a result, two scene generation devices (SGDs) are usually employed to generate spectrally separated images. And they are fused and projected onto the UUT. Two kinds of SGDs are usually used in dual-band IRSP, resistor array and digital micro-mirror device (DMD).

The resistor array is a mature technology. Early representative systems based on two resistor arrays include the Kinetic Kill Vehicle hardware-in-the-loop simulation (KHILS, 2004) facility from the Eglin Air Force Base, and the Seeker Experimental System (SES, 2006) within Optical System Test Facility (OSTF) from the Massachusetts Institute of Technology (MIT) Lincoln Laboratory [8,9]. Currently, the most representative dual-band IRSP is designed by Santa Barbara Infrared (SBIR) in 2013, employing two newest MIRAGE-XL resistor arrays [10,11]. These IRSPs usually cover atmospheric bands from short wave infrared (SWIR) to long wave infrared (LWIR), using the reflective off-axis optical structure to avoid chromatic aberration correction. However, they still have obvious shortcomings such as poor uniformity, complex thermal control in the aspect of device and high fabrication cost, difficult alignment and testing.

DMD has the advantages of its wide spectral response, high spatial resolution, good uniformity, and low device cost. Two-DMD based dual-band IRSPs are usually designed as refractive type to satisfy the lighting requirements of DMD [12]. In addition to considering the chromatic aberration caused by wide spectral bands, this optical structure overcomes main shortcomings of the configuration based on resistor array. Accordingly, the two-DMD based IRSP designed by Optical Sciences Corporation (OSC, 2009) or OPTRA Inc. (2012) only operates in two sub-bands of medium wave infrared (MWIR) [13–15]. They apply to test MWIR threat detection system, such as missile warning system, severely restricting the scope of application.

In our dual-band IRSP, we use two DMDs to compose the scene

* Corresponding author.
E-mail address: panyue@cust.edu.cn (Y. Pan).

https://doi.org/10.1016/j.infrared.2019.103164
Received 22 September 2019; Received in revised form 17 December 2019; Accepted 18 December 2019
Available online 20 December 2019
1350-4495/

generation module, which is used in MWIR and LWIR regions in conjunction with two illumination modules and a common telecentric projection module. It overthrows an inertial thinking that the MWIR and LWIR dual-band IRSP is designed by using resistor array based reflective optical structure, significantly reducing fabrication cost and the difficulty of alignment and testing. Meanwhile, it greatly improves the quality of projected image. Except for the difficult correction of chromatic aberration, we are also faced with another serious problem, that is, the great difference of thermal properties between IR-transmitting glass and metallic materials. Simultaneously, considering the temperature change in the periods of operation, fabrication, and alignment, we should reasonably predict the suitable operating temperature range for improving the temperature adaptability of the IRSP.

In this paper, the opto-mechanical design of the IRSP is first discussed in detail. The temperature adaptability of illumination and projection assemblies are analyzed by finite element analysis (FEA). Then the heat induced deformation data of the IRSP is analyzed with Zernike polynomials, with the optical performance being evaluated by ray-tracing software. The preliminary results of laboratory tests are presented finally.

2. Opto-mechanisms design of the IRSP

The schematic diagram of our dual-band IRSP is depicted in Fig. 1. The illumination modules have the same opto-mechanical structure and specific bandpass filters (BPFs) corresponding to each infrared band. Two DMDs are synchronously controlled to generate images of different bands at the same time. By using thermoelectric coolers, the window of DMD is temporarily stabilized below 2 °C, which is the dew point of the experimental environment. The main specifications of the IRSP are listed in Table 1.

The tilt angle of DBC relative to projection axis is 30°. According to Snell's law, the MWIR DMD is mounted on a 30° angled mounting plate (bracket). And the LWIR DMD is mounted on the six-axis stages for adjusting the relative position between DMDs to register the images. After adjusting, axes of DMDs and DBC are coplanar with projection axis. The square micro-mirrors of DMD flip +12° or −12° around the diagonal. In order to enable the "on" state beam to exit along the projection axis, the elevation angle between the illumination axis and DMD axis is 24°, and the azimuth angle is 45°, as shown in Fig. 2(a).

Accordingly, as shown in Fig. 2(b), the LWIR illumination module is mounted on a 45° angled mounting plate, while the MWIR illumination module is mounted on a combined bracket consisting of 60° and 45° angled mounting plates. And they are located on both sides of the projection axis. In addition, all the customized brackets are machined from one solid extruded shape, and every mounting surface has been precision-machined to achieve ± 1 arcmin angular tolerance and 0.025 mm flatness.

Table 1
Specifications and performances of the IRSP.

Parameter	Value
Spectral ranges	3.7–4.8 μm and 8–12 μm
Field of view	± 3.75° and ± 1.875°
Focal length	133.6 mm and 267.2 mm
Image contrast	200:1 (MWIR); 10:1 (LWIR)
Max apparent temperature[a]	≥600 K (MWIR); ≥400 K (LWIR)
Video interface	VGA; HDMI
Array size of DMD	1024 × 768
Pixel pitch of DMD	13.68 μm
Sensor area of DMD	14.1 mm × 10.5 mm

[a] The IRSP apparent temperature is dependent on the temperature of blackbody source, and the temperature range is determined by the simulated scenes.

2.1. Optimized opto-mechanisms design of illumination module

The housing of the illumination module is also machined from one solid, which is similar to the angled mounting plate, and all the mounting surfaces are precisely machined to achieve the desired accuracy. The realized design of the illumination module is presented in Fig. 3. The flat mirrors with 6:1 diameter-to-thickness ratio are integrally designed with the mirror mounts. In order to have the same CTEs for different components, the mirrors, mounts and housing are made of the same material. For isolating the optical surface from the mounting surface, there is a ring slot on the circumference of the mirror. And a circular groove is machined on the mirror's mounting surface, significantly reducing the precision machining area. There are three parallel mounting pads with thread holes on the mount, which are used to keep the mirror in normal position and connect to the housing. In addition, by single point diamond turning (SPDT), the proper flatness of all mounting surfaces, especially optical surfaces, can be ensured [16,17].

The blackbody shell temperature will rise to about 45 °C during operation, and the lens 2(9) is heated slowly by continuous irradiation, which will lead to the change of the axial temperature gradient of illumination module. A FEA model is used for predicting the adaptability of the structure to the axial temperature loading, and the heat source is set on the blackbody exit surface. Taking LWIR as an example, after introducing the thermal environment, initial conditions, and boundary conditions to the FEA model, the temperatures at all mesh points are calculated to obtain the temperature distribution, which is shown in

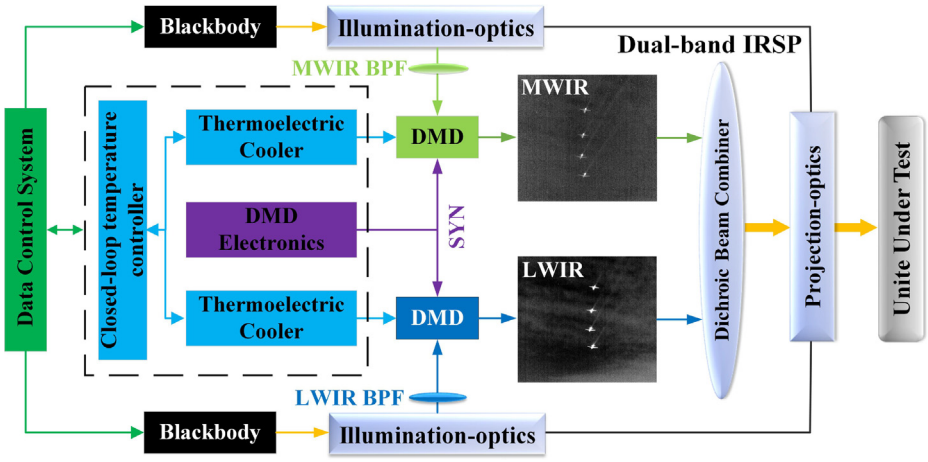

Fig. 1. Schematic of the two-DMD based dual-band IRSP.

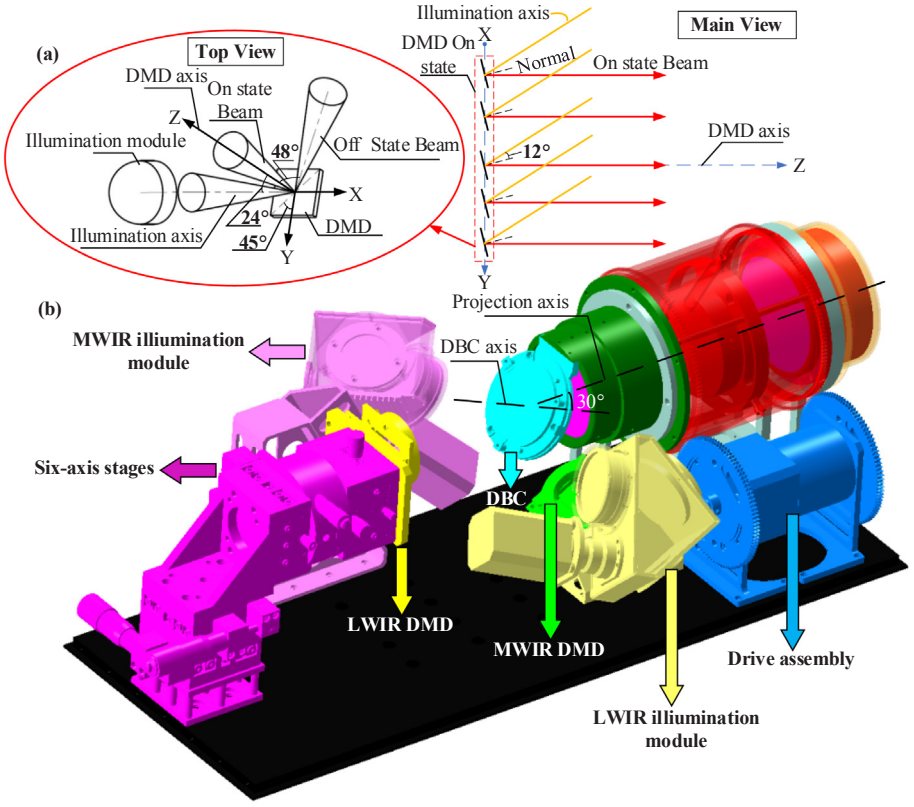

Fig. 2. Opto-mechanical structure and spatial layout of the IRSP. (a) A simplified local space coordinate system is established to show the spatial angle between incident beam and exiting beam of DMD. (b) Opto-mechanical system of the IRSP.

Fig. 4(a). The materials of lens and mirrors are germanium and aluminum respectively, and the material properties are shown in Table 4 in the next section.

It can be seen that the increase of temperature mainly concentrates on the position of lens 2(9). But temperatures on other positions are stabilized below 25 °C, close to initial temperature. The reason is that the optical elements are discretely mounted on the housing, significantly reducing the heat transfer between each other. The non-uniform temperature field causes the structure to deviate away from the nominal defined shape, so we perform the stress-strain analysis according to the obtained temperature field. The reference temperature for the undeformed illumination module is assumed to be 20 °C. As shown in Fig. 4(b), the displacements of mesh points for the optical elements are less than 8 μm.

Considering the additional impact of ambient temperature change, the elastomeric mounting is used to fix the lens near the source [18]. As shown in Fig. 3, the lens (2)9 is held in place by the fixture to align within the cell 1, then the elastomer is injected into radially oriented holes until the space around the lens is filled. Furthermore, the machined surface of the fixture is coated with mode release, thereby the

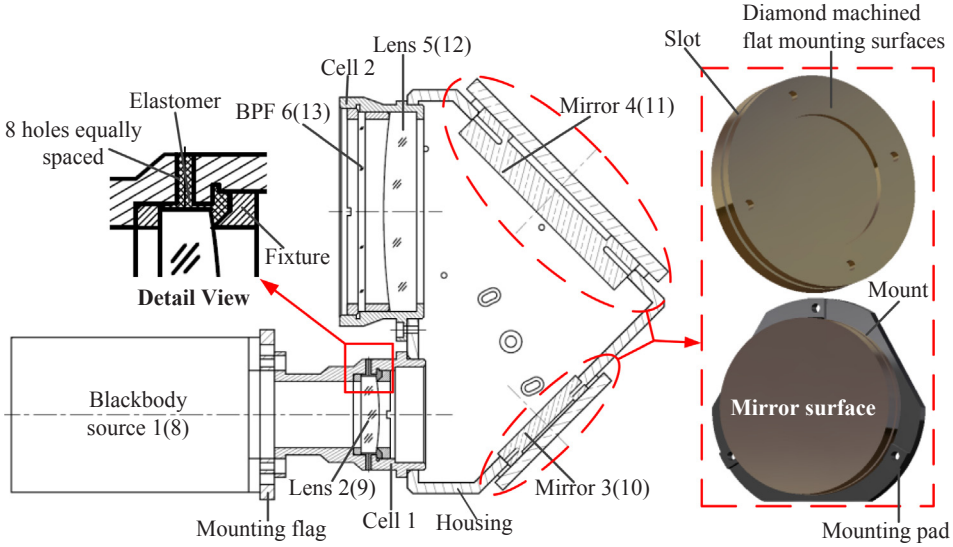

Fig. 3. The detail configuration and cross section of the illumination module. All axes are coplanar. The axes of the lenses are parallel, the axes of the mirrors are perpendicular, and the axial angle between lens and mirror is 135°.

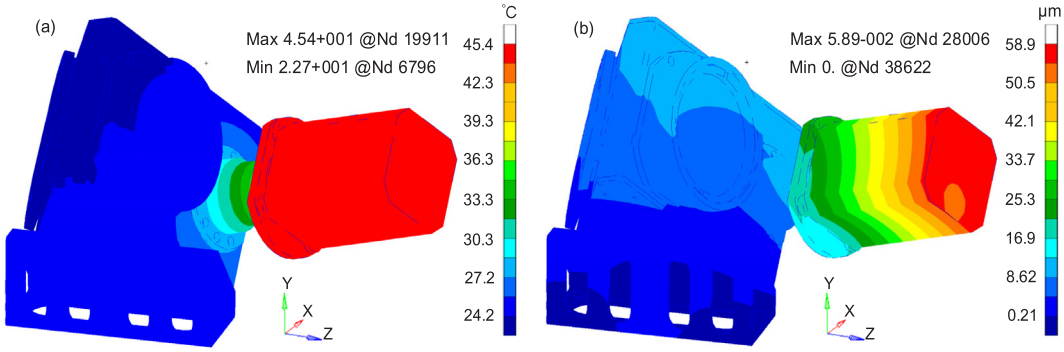

Fig. 4. Thermal analysis of illumination module based on FEA model. (a) Temperature field change induced by axial temperature loading. (b) Thermally induced structural deformation.

fixture can be removed after curing. The elastomeric ring can minimize stress buildup within the optical element caused by axial temperature loading. The axial length of the elastomer layer equals the edge thickness of the lens, and the particular thickness of the elastomer is given by:

$$t_e = \frac{D_l(1-\nu_e)(\alpha_c-\alpha_l)}{2[\alpha_e-\alpha_c-\nu_e(\alpha_l-\alpha_e)]} \tag{1}$$

where D_l is the diameter of the lens, ν_e is the Poisson's ratio of the elastomer layer. Besides, α_e, α_c and α_l are the CTEs of the elastomer, lens and cell, respectively. When subjecting to radial gravitational loading, the decentration of the lens is expressed as:

$$\delta_l = \frac{2m_l t_e}{\pi D_l t_l E_e[(3-2\nu_e)/(1-\nu_e^2)]} \tag{2}$$

where m_l is the lens weight, t_l is the edge thickness of the lens, E_e is the elastomer Young's modulus. The calculation parameters of Eqs. (1) and (2) are given in Table 2.

From Eq. (1), the radial thickness of elastomer layer t_e is 0.742 mm, but the actual thickness is 0.8 mm instead of the calculated value, which is a design choice. From Eq. (2), the calculated decentration of the lens 2(9) δ_l is 0.0478 μm under radial gravitational loading, which can be ignored for reducing the illumination uniformity.

2.2. Opto-mechanisms design of projection module

The projection module is mainly composed of the DBC, projection lens, stepper motor, encoder, and the brackets. As shown in Fig. 5(a), all the lenses are assembled in respective barrels by optical centering processing and assembling technology. As for the rear fixed group, the air space between lens 16 and 17 is too small for a separator, whose solution is that the lenses are respectively bonded to the cells by injecting a ring of 3M 2216 epoxy, then the air space is controlled by the separator between cells. The similar method is adopted to control the air space between lens 17 and 18. Furthermore, the metal-to-glass interface on convex surfaces is machined on a tangent plane to reduce installation stress.

The DBC is mounted on the projection lens by the angled mounting plate, which is considered as a flexible plane-parallel plate. Accordingly, the semi-kinematic mounting is chosen for DBC, as shown in Fig. 5(b). There are six flat pads with threaded holes symmetrically distributed on both sides of the base plate. And the DBC is pressed against the three pads on one side by three spring clips. The base plate is installed on the angled mounting plate via other three pads for eliminating the bending moments introduced by the localized irregularities on the supporting surface as far as possible. In addition, the clips are designed as cantilevered beams, with the minimum preload imposed by the clips being given by:

$$F_{\min} = m_D f_s a_\Sigma \tag{3}$$

where m_D is the weight of the DBC, f_s is the safety factor that is usually equal to 2, and a_Σ is the total acceleration caused by gravity and dynamic loadings. From Eq. (3), the required minimum preloads $F_{\min}$ is 1.590 N, and the corresponding deflection of a spring clip is determined as:

$$\Delta = (1-\nu_c^2)(4F_{\min}L^3)/(E_c b t_c^3 N) \tag{4}$$

where ν_c and E_c are material Poisson's ratio and Young's modulus respectively, L is the clip's free length, b and t_c are the width and the thickness of the clip respectively, and N is the quantity of employed clips. The stress caused by deflection is calculated by:

$$S_\Delta = 6F_{\min}L/(bt_c^2 N) \tag{5}$$

The calculation parameters of Eqs. (4) and (5) are given in Table 3. According to Eq. (4), the deflection Δ is 0.012 mm when imposing the minimum preloads. From Eq. (5), the corresponding stress within the clip S_Δ is 15.27 MPa. The realized value of Δ should be greater than the minimum, and the actual value is specified as 0.1 mm. Because the relationship is linear between the defection and the stress, the value of S_Δ is deduced as 127.25 MPa, which is much less than the material (Spring steels) yield strength 343 MPa. Although the DBC is insensitive to lateral motions, we still use three pegs made of polytetrafluoroethylene (PTFE) to avoid excessive displacement.

3. Opto-thermal analysis of the projection lens

Based on the principle of energy conservation and Fourier's law, the temperature distribution of subject can be expressed by the second order partial differential equation as follow [19]:

$$c_p\rho\frac{\partial T}{\partial \tau} = k\left(\frac{\partial^2 T}{\partial x^2}+\frac{\partial^2 T}{\partial y^2}+\frac{\partial^2 T}{\partial z^2}\right)+Q_v(x,y,z;\tau) \tag{6}$$

Table 2
Calculation parameters of Eqs. (1) and (2).

Lens 2(9)				Elastomer layer			Cell 1
Diameter D_l (mm)	Weight m_l (kg)	Edge thickness t_l (mm)	CTE α_l (°C^{-1})	Poisson's ratio ν_e	CTE α_e (°C^{-1})	Young's modulus E_e (MPa)	CTE α_c (°C^{-1})
22	8.35×10^{-3}	4	6.1×10^{-6}	0.499	300.6×10^{-6}	3.448	23.6×10^{-6}

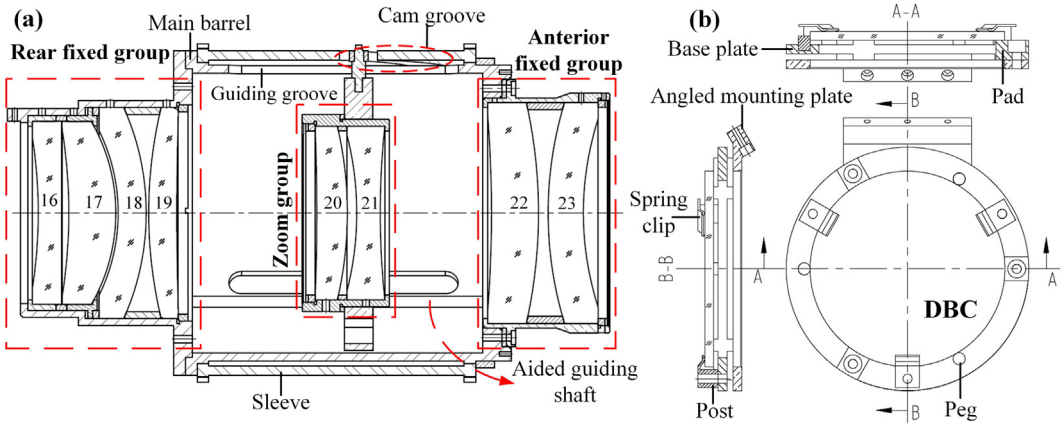

Fig. 5. The detail configuration and cross section: (a) projection lens and (b) DBC.

where c_p is the heat capacity, ρ is the density, T is the temperature, k is the thermal conductivity, where $\partial T/\partial \tau$ represents that temperature changes with time, $\partial T/\partial x$, $\partial T/\partial y$ and $\partial T/\partial z$ represent temperature gradients respectively, and where Q_v represents the heat source term.

DMD chip is the only potential heat source on the axis of projection lens. However, it can be eliminated by dissipating heat back, not being connected to the projection lens and controlling thermal accumulation effect via thermoelectric coolers. Accordingly, we can infer the heat source term Q_v is equal to 0. In addition, the coating on the lens absorbs about 2% of radiant flux and converts into heat, which is much less than exchanging heat with ambient air. Accordingly, it can be seen that the heat loss or gain is mostly driven by ambient temperature, and the heat conduction only occurs between the bottom of bracket and the optical bench.

It is assumed that under different environmental conditions, the temperature range is 10–40 °C and the duration is twelve hours. Since there is no additional heat source, such temperature variation is obviously isotropic. The convection coefficient is set as a variable field distribution. And the conduction coefficient is treated as a constant because the surface temperature of the optical bench is almost constant. According to the conditions of heat transfer, the calculated temperature distribution of projection lens is shown in Fig. 6(a). The non-uniformity of temperature distribution is caused by the differences between physical properties of materials. When heat is transferred to different parts of the projection assembly, thermal strain is built up, resulting in structural deformation. For isotropic linear elastic solid, the thermal strain is given by:

$$\varepsilon = \alpha[T(\tau) - T_0] \tag{7}$$

where α is CTE of the material, $T(\tau)$ is instantaneous temperature, and T_0 is the stress-free initial temperature. The temperatures of optical elements averagely increase by 15 °C. According to Eq. (7), Q345 steel is more reasonable than 6061 Al as the elastic holding material of DBC, which can effectively avoid the loosening caused by temperature change.

The ambient temperature changes slowly, thereby the method of quasi-static processing is used for analyzing the non-stationary thermal-stress. Namely the ambient temperature changing process is decomposed a series of heat steady states to get the structural response according to the temperature distribution that corresponds to each time step. We impose the temperature field on the structural model of projection lens, and calculate the displacement of the grid point through the solver, as shown in Fig. 6(b).

It can be seen that the thermally induced displacements of metallic elements are larger than the optics due to the difference of material CTEs. And the displacements of mesh points are all less than 5 μm for optical elements, which shows the opto-mechanisms design of projection lens is reliable within the current temperature range. The standard values of the material properties used in FEA are listed in Table 4 [20].

The thermally induced displacement data obtained from FEA need to convert to sag deformation values for evaluating the optical performance. The nominal shape of each optical surface is defined as:

$$s = \frac{c\rho^2}{1 + \sqrt{1 - (K+1)c^2\rho^2}} + \sum_i a_i \rho^{2i} \tag{8}$$

where a_i represents the coefficient of even aspheric surface (i = 1, 2, 3, …), s the surface sag, c the surface vertex curvature, K the conic constant, and ρ the radial position. The sag deformation is expressed as [21]:

$$\Delta s = \Delta z - \frac{\partial s(\rho_0)}{\partial \rho}\sqrt{\Delta x^2 + \Delta y^2} \tag{9}$$

where Δx, Δy, Δz are components of displacement vector along x, y and z direction respectively. The projection lens has 18 optical surfaces. Taking the aspheric surfaces for example, the converted sag deformation date from Eq. (9) can be fitted in terms of Zernike polynomial as:

$$\Delta s(\rho, \phi) = \sum_{j=1}^{\infty} a_j Z_j(\rho, \phi) \tag{10}$$

where ϕ represents the azimuth angle, a_j represents the coefficient of each Zernike term (j = 1, 2, 3, …). The ability of Zernike polynomials is limited on capturing high-frequency surface imperfections, thus only the first 37 terms of standard Zernike are used for high-accurate fitting. When M sample mesh nodes are selected, the coefficients a_j of Zernike terms are computed by:

Table 3
Calculation parameters of Eqs. (4) and (5).

Geometry of spring clip			Physical properties		
Free length L (mm)	Width b (mm)	Thickness t_c (mm)	Poisson's ratio ν_c	Young's modulus E_e (MPa)	Number of clips N
12	10	0.5	0.31	2.12×10^5	3

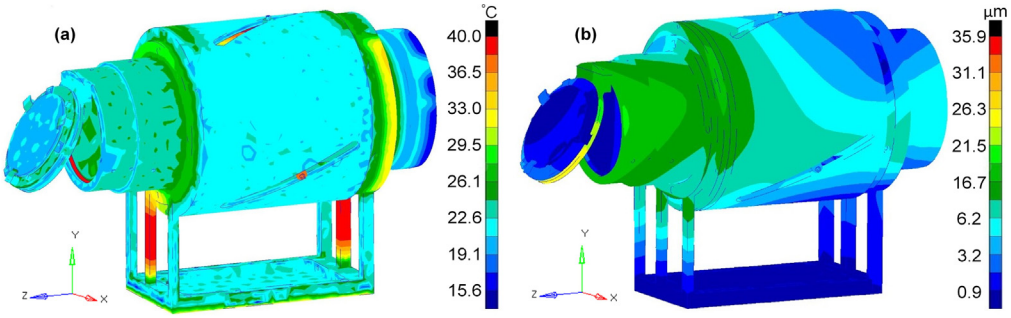

Fig. 6. The impact of heating on projection lens when ambient temperature varies between 10 °C and 40 °C. (a) Temperature distribution. (b) Thermally induced structural deformation. The displacements at the bottom boundary of the bracket are kept fully constrained.

Table 4
Material properties of main components.

Component	Material	Conductivity (W/m·K)	CTE ($°C^{-1}$)	Young's modulus (MPa)	Density ($g·cm^{-3}$)	Specific heat (J/kg·K)	Poisson's Ratio
Lens 18	Ge	59	6.1×10^{-6}	10,370	5.32	30.98	0.278
Lens 23, 16	ZnS	17	6.6×10^{-6}	7450	4.08	46.88	0.290
Lens17, 19, 21, 22	AMTIR-1 ($Ge_{33}As_{12}Se_{55}$)	0.26	12.0×10^{-6}	2200	4.49	29.30	0.266
Lens 20 and DBC 15	ZnSe	18	7.1×10^{-6}	70,300	5.27	33.91	0.280
Major opto-mechanics	6061 Al	167	23.6×10^{-6}	68,200	2.68	960	0.332
Main Barrel and Sleeve	40Cr Steel	32.6	11.0×10^{-6}	205,800	7.85	460	0.30
Spring Clip	Q345 Steel	48	11.26×10^{-6}	212,000	7.85	480	0.31

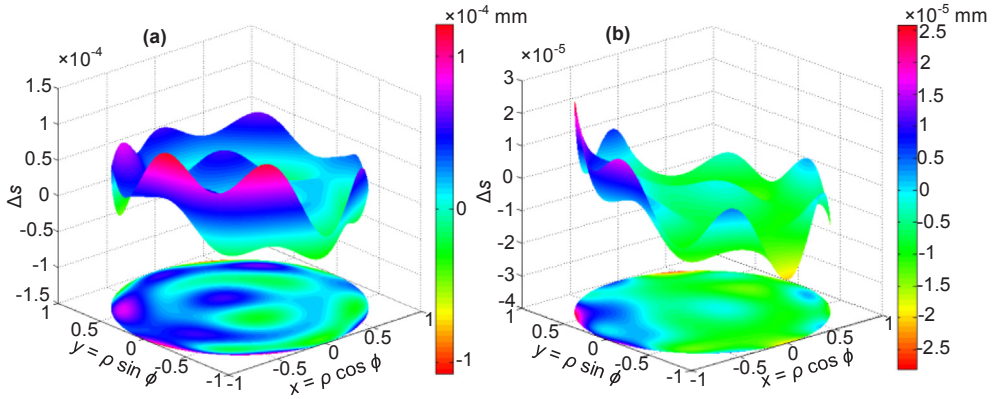

Fig. 7. Thermally induced deformation: (a) aspheric surface 1 and (b) aspheric surface 2. The fitting results are mapped to the bottom to better show sag deformations on optical surfaces.

$$\begin{cases} a_1 Z_1(\rho_1, \phi_1) + a_2 Z_2(\rho_1, \phi_1) + \cdots + a_{37} Z_{37}(\rho_1, \phi_1) = \Delta s_1 \\ a_1 Z_1(\rho_2, \phi_2) + a_2 Z_2(\rho_2, \phi_2) + \cdots + a_{37} Z_{37}(\rho_2, \phi_2) = \Delta s_2 \\ \vdots \\ a_1 Z_1(\rho_M, \phi_M) + a_2 Z_2(\rho_M, \phi_M) + \cdots + a_{37} Z_{37}(\rho_M, \phi_M) = \Delta s_M \end{cases} \quad (11)$$

Eq. (11) is a contradictory equation that only has the optimal solution, so we use the least squares algorithm to solve the values of a_j by MATLAB. According to Eq. (11), the residuals equation is written as [22]:

$$\begin{cases} a_1 Z_1(\rho_1, \phi_1) + a_2 Z_2(\rho_1, \phi_1) + \cdots + a_{37} Z_{37}(\rho_1, \phi_1) - \Delta s_1 = \Delta_1 \\ a_1 Z_1(\rho_2, \phi_2) + a_2 Z_2(\rho_2, \phi_2) + \cdots + a_{37} Z_{37}(\rho_2, \phi_2) - \Delta s_2 = \Delta_2 \\ \vdots \\ a_1 Z_1(\rho_M, \phi_M) + a_2 Z_2(\rho_M, \phi_M) + \cdots + a_{37} Z_{37}(\rho_M, \phi_M) - \Delta s_M = \Delta_M \end{cases} \quad (12)$$

The objective function is

$$F = \min \sum_{i=1}^{M} \Delta_i^2 \quad (13)$$

When objective function reaches the minimum value at the inflection point, the optimal solution about all coefficients a_j can be obtained.

The thermally induced deformation fitting results of aspheric surfaces are shown in Fig. 7. The sag deformation of aspheric surface 1 is at the 0.1 μm magnitude, and aspheric surface 2 is one order magnitude smaller than the surface 1. Considering the results of thermally induced structural deformation, the conclusion is drawn that the distribution of sag deformation is within a reasonable range.

The coefficients of all nine lens are directly imported into a commercial ray tracing software Zemax. And the optical performance of the projection lens is evaluated in term of the MTF. It is worth noting that the most serious thermally induced deformations usually occur when the ambient temperature reaches its minimum or maximum value.

The pixel pitch of DMD is 13.68 μm corresponding to the cutoff frequency of MTF is about 36.5 cycles per mm (C/mm). In the test of HWIL simulation, the image of DMD is mapped to the sensor area of the detector of the UUT. The pixel pitch of the detector is 35 μm and the corresponding cutoff frequency is about 14.3 C/mm, which means that the IRSP is a detector limited system. According to the angular resolution relation determined by the mapping relation between the IRSP and the UUT, the relative pixel pitch of DMD can be expressed as:

$$P_{DMD} = f_{IRSP} \cdot P_{Dec} / f_{UUT} \quad (14)$$

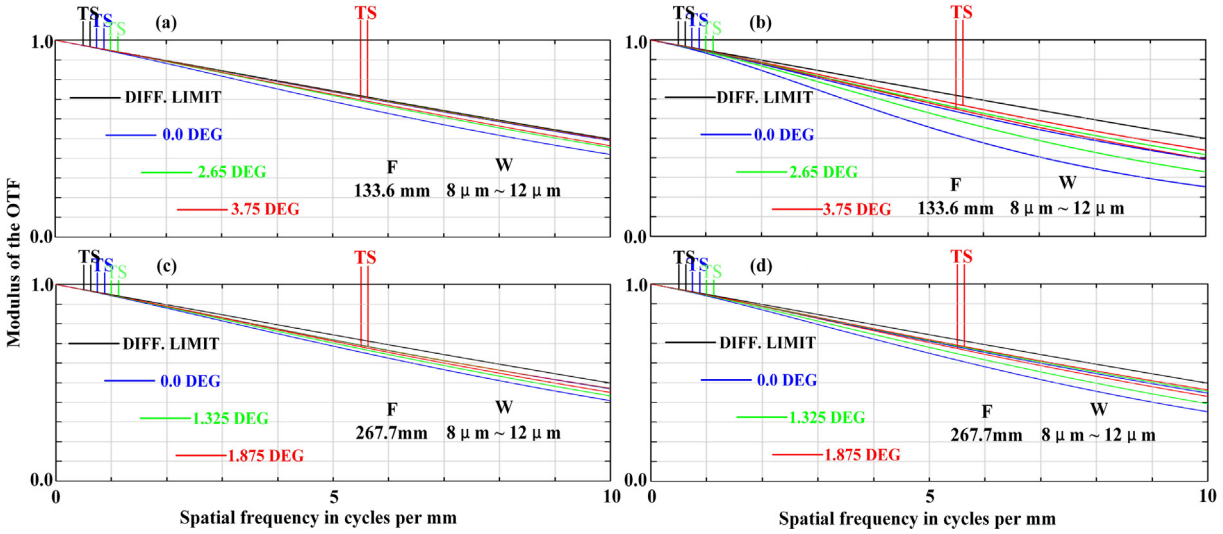

Fig. 8. MTF of the projection lens in band of 8–12 μm with (a) short focus at 10 °C, (b) short focus at 40 °C, (c) long focus at 10 °C and (d) long focus at 40 °C. T denotes meridional field of view, and S denotes sagittal field of view.

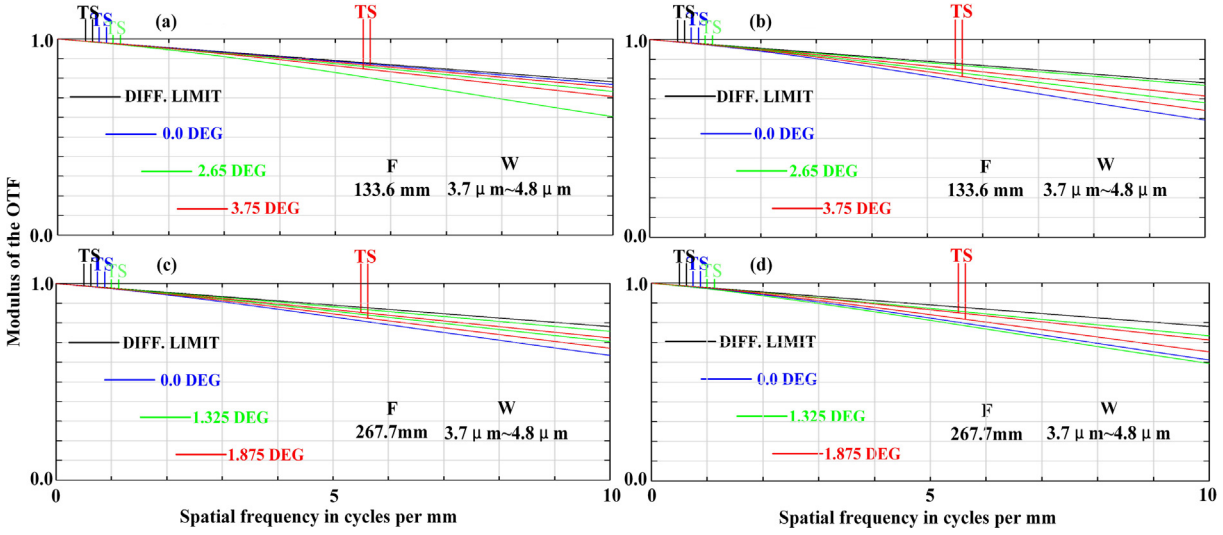

Fig. 9. MTF of the projection lens in band of 3.7–4.8 μm with (a) short focus at 10 °C, (b) short focus at 40 °C, (c) long focus at 10 °C and (d) long focus at 40 °C. T denotes meridional field of view, and S denotes sagittal field of view.

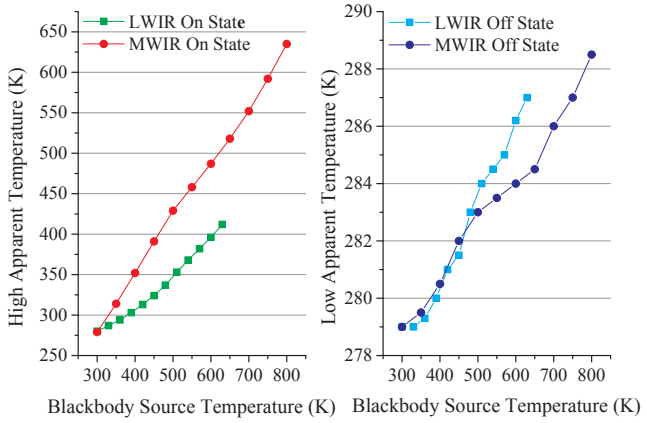

Fig. 10. Measured apparent temperature of the IRSP.

where f_{IRSP} is the focal length of the IRSP, f_{UUT} the focal length of the UUT, and P_{Dec} the pixel pitch of the detector. The fact is that f_{IRSP} is about twice as long as f_{UUT}. According to Eq. (14), we can obtain the value of P_{DMD} that is approximately 70 μm, showing that the cutoff frequency is about 7 C/mm. Therefore, we select 10 C/mm as the cutoff frequency.

As shown in Fig. 8(a) and (c), in band of 8–12 μm, the values of modulus are all better than 0.4 at 10 C/mm when the temperature is 10 °C. However, when the temperature rises to 40 °C, the MTF curves drop significantly, especially for 0°-FOV shown in Fig. 8(b) and (d), the values of modulus reduce by 33.7% and 15.7% at 10 C/mm, respectively. As shown in Fig. 9(a)–(d), in band of 3.7–4.8 μm, whether the temperature is 10 °C or 40 °C, the values of modulus are always better than 0.6 at 10 C/mm, which implies that the projection performance is insensitive to the current temperature range in MWIR band. In summary, during operation of the IRSP, the suggested ambient temperature should be stabilized below 35 °C, which is enough to keep the thermal distortions within tolerable limits.

4. Preliminary performance evaluation

Two high-accuracy thermal imagers with different bands are used to preliminarily test the performance of the IRSP under the suitable

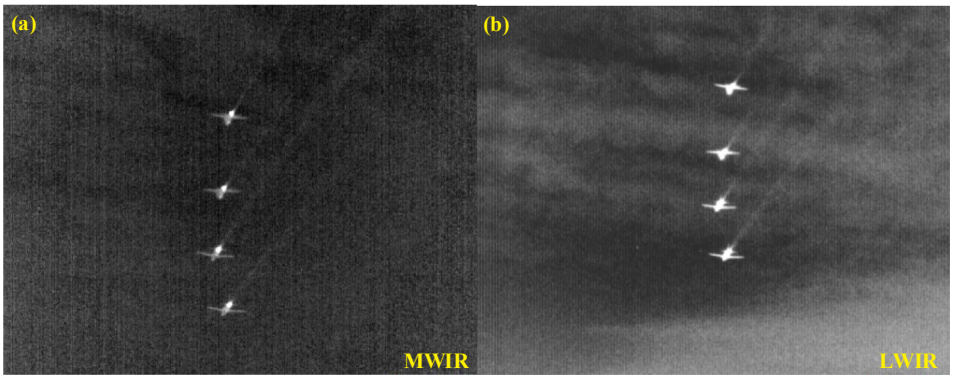

Fig. 11. Projected images (a) MWIR (b) LWIR.

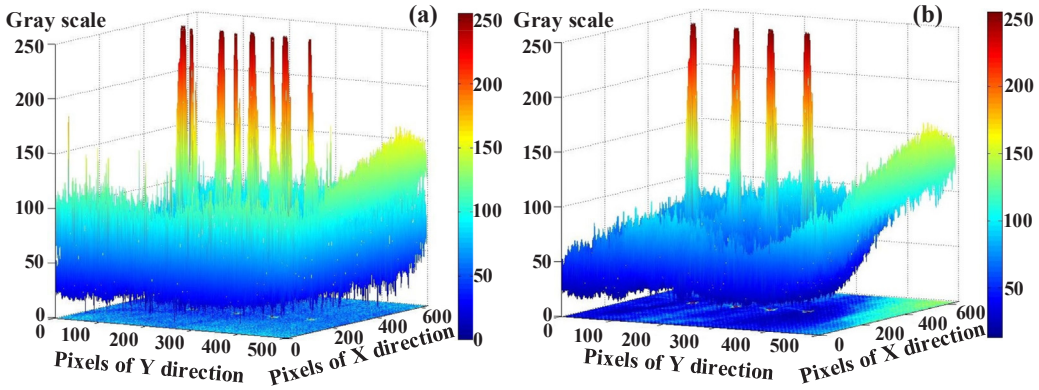

Fig. 12. Grayscale distribution (a) MWIR (b) LWIR.

ambient temperature. The testing results of apparent temperature are shown in Fig. 10, with the sampling interval being set as 50 K. When temperature of blackbody source rises to 608 K, high apparent temperature reaches the required 400 K in LWIR band. The desired high apparent temperature is 600 K in MWIR band, correspondingly, the blackbody temperature is 813 K. The high apparent temperature depends on the blackbody, but the low apparent temperature is determined by stray light control of the IRSP. Because thermoelectric coolers have effectively controlled DMD temperature, corresponding low apparent temperatures only rise by 7.8 K and 9.5 K respectively in the process of increasing blackbody temperature.

When temperatures of both blackbody sources are set to 800 k, end-to-end imaging results are shown in Fig. 11(a) and (b). We can find that the image quality in LWIR band is lower due to the diffraction of DMD chip in LWIR band by comparing images. For our IRSP, the long projection entrance pupil distance required by direct lighting mode has effectively prevented the mostly diffraction energy from entering the projection lens. Conversely, if the field lens or TIR prism is used in the IRSP, the quality of LWIR image would be much lower.

By traversing all the pixels in images of Fig. 11, the grayscale distributions of images are obtained respectively. As can be seen from Fig. 12(a), in the MWIR image, the minimum gray value is 1, and the maximum value is 242. As shown in Fig. 12(b), the minimum gray value is 22, and the maximum is 244 in the LWIR image. Consequently, the contrasts of the images in two bands are better than the requirements specified in Table 1. If we increase the blackbody temperature, the maximum gray value will increase to 255, while the contrast will be further reduced.

5. Conclusion

The dual-band IRSP based on two DMDs discussed and evaluated in this paper is a practical instrument for testing various infrared imaging systems in HWIL simulation. The opto-mechanism of IRSP is designed to take full account of temperature adaptability. The lens near the source is held in place with elastic mounting, and all the mirrors manufactured by means of SPDT are opto-mechanical integrated design. The influence of temperature loading on opto-mechanical system is predicted by opto-thermal FEA. And the sequential ray-tracing analysis shows that the ambient temperature should be stabilized below 35 ˚C during the operation of IRSP, which is easily achieved under ordinary conditions. Preliminary laboratory tests have indicated that IRSP has great potential in HWIL simulation under appropriate ambient temperature.

Funding

National Natural Science Foundation of China (61903048).

Declaration of Competing Interest

We stated that there is no conflict of interest. We have purchased the genuine license of the software used in our article. And the material data in the tables is obtained from open channels and have been add in the references.

References

[1] D.A. Saylor, J. Terry, J. Morris, Infrared and semi-active laser simulation capabilities at the multi-spectral system simulation (MSS) HWIL facility, Proc. SPIE 6492 (2008) 649209.
[2] C. Fink, New technologies for HWIL testing of WFOV, large-format FPA sensor systems, Proc. SPIE 9820 (2016) 98201B.
[3] N.J. Pollica, C.C. Alexay, Wide-angle catadioptric optics for broadband applications, Proc. SPIE 8704 (2013) 87042A.
[4] A. Bodkin, A. Sheinis, J. McCann, Compact multi-band (VIS/IR) zoom imaging system for high resolution long range surveillance, Proc. SPIE 5783 (2005) 816–826.

[5] Oliver Schreer, Mónica López Sáenz, Christian Peppermüller, Uwe Schmidt, Dual-band camera system with advanced image processing capability, Proc. SPIE 6542 (2007) 65421C.
[6] S. Coudrain, M. Bernhardt, R. Caes, Y. Domel, R. Ferrec, D. Gouyon, M. Henry, A. Jacquart, P. Kattnig, L. Perrault, L. Poutier, M. Rousset-Rouvière, M. Tauvy, S. Thétas, J. Primot, SIELETERS, an airborne infrared dual-band spectro-imaging system for measurement of scene spectral signatures, Opt. Express 23 (12) (2015) 16164–16176.
[7] O. Cocle, C. Rannou, B. Forestier, P. Jougla, P.F. Bois, E.M. Costard, A. Manissadjian, D. Gohier, QWIP compact thermal imaging system: catherine-XP and its evolution, Proc. SPIE 6542 (2007) 654234.
[8] R.A. Thompson, W.L. Herald, T.P. Bergin, S.A. Marlowb, E.W. Glattkeb, Advances in cryo-vacuum test capabilities for dual-band sensors at the kinetic kill vehicle hardware-in-the-loop simulation (KHILS) facility, Proc. SPIE 5408 (2004) 107–117.
[9] David C. Harrison, Alexander G. Hayes, Leaf A. Jiang, Eric L. Hines, Jonathan M. Richardson, The MIT Lincoln laboratory optical systems test facility, Proc. SPIE 6208 (2006) 620801.
[10] J. LaVeigne, G. Franks, M. Prewarski, A 2-color 1024x1024 dynamic infrared scene projection system, Proc. SPIE 8707 (2013) 870703.
[11] J. LaVeigne, G. Franks, Tom Danielson, Thermal resolution specification in infrared Scene projectors, Proc. SPIE 9452 (2015) 94520Y.
[12] Yang Qiao, Xu. Xiping, Tao Liu, Yue Pan, Design of a high-numerical-aperture digital micromirror device camera with high dynamic range, Appl. Opt. 54 (1) (2015) 60–70.
[13] D. Brett Beasley, Matt Bender, Jay Crosby, Tim Messer, Dynamic infrared scene projectors based upon the DMD, Proc. SPIE 7210 (2009) 72100I.
[14] Julia Rentz Dupuis, David J. Mansur, Robert Vaillancourt, Two-band DMD-based infrared scene simulator, Proc. SPIE 7663 (2010) 766302.
[15] David J. Mansur, Robert Vaillancourt, Ryan Benedict-Gill, Scott P. Newbry, Julia Rentz Dupuis, High dynamic range digital micromirror device-based infrared scene projector, J. Micro/Nanolithogr. MEMS MOEMS 13 (1) (2014) 011102.
[16] Zhaohui Li, Bo Chen, Kefei Song, Xiaodong Wang, Shijie Liu, Liang Yang, Hu Qinglong, Ke Qiao, Liping Zhang, Wu Guodong, Yu Ping, Opto-mechanisms design of extreme-ultraviolet camera onboard Chang E lunar lander, Opt. Express 22 (13) (2014) 15932–15940.
[17] Liyin Yuan, Zhiping He, Gang Lv, Yueming Wang, Chunlai Li, Jia'nan Xie, Jianyu Wang, Optical design, laboratory test, and calibration of airborne long wave infrared imaging spectrometer, Opt. Express 25 (19) (2017) 22440–22454.
[18] Paul R. Yoder Jr., 2006. Opto-Mechanical System Design, third ed. CRC Press, Chap. 4.
[19] Ravinder K. Banyal, B. Ravindra, S. Chatterjee, Opto-thermal analysis of a light-weighted mirror for solar telescope, Opt. Express 21 (6) (2013) 7065–7081.
[20] Huaizhi Yu, 2015. Infrared Optical Material, second ed. National Defense Industry Press, Chap. 2 and Chap. 3.
[21] Victor Genberg, Gregory Michels, Opto-mechanical analysis of segmented/adaptive optics, Proc. SPIE 4444 (2001) 90–101.
[22] Xifa Song, Lin Li, Yifan Huang, Method of determining effects of heat-induced irregular refractive index on an optical system, Appl. Opt. 54 (25) (2015) 7701–7707.